Earthquake ruptures and topography of the Chilean margin controlled by plate interface deformation

Nadaya Cubas[1], Philippe Agard[1], and Roxane Tissandier[2]

[1]Sorbonne Université, CNRS-INSU, Institut des Sciences de la Terre Paris, ISTeP UMR 7193, F-75005 Paris, France
[2]Institut de Physique du Globe de Paris, Université de Paris, CNRS, 75238 Paris, France

Correspondence: Nadaya Cubas (nadaya.cubas@sorbonne-universite.fr)

Abstract. What controls the location and segmentation of mega-earthquakes in subduction zones is a long-standing problem in earth sciences. Prediction of earthquake ~~ruptures~~ rupture extent mostly relies on interplate coupling models based on Global Navigation Satellite Systems providing patterns of slip deficit between tectonic plates. We here investigate if and how the ~~seismic and aseismic~~ strongly and weakly coupled patches revealed by these models relate to the distribution of deformation along the plate interface, i.e. basal erosion and/or underplating. From a mechanical analysis of the topography applied along the Chilean subduction zone, we show that extensive plate interface deformation takes place along most of the margin. We show that basal erosion occurs preferentially at 15 km depth while underplating does at 35 ± 10 and 60 ± 5 km depth, in agreement with P-T conditions of recovered underplated material, expected pore pressures, and spatial distribution of marine terraces and uplift rates. ~~Along southern Chile~~ South of the Juan Fernandez Ridge, large sediment input favors shallow accretion and underplating of subducted sediments, while along northern Chile, extensive basal erosion provides material for the underplating. We then show that ~~all major earthquakes of southern Chile~~ , along the accretionary margin, the two last major earthquakes are limited along their down-dip end by underplating while, along ~~northern Chile~~ the erosive margin, they are surrounded by both basal erosion and underplating. Segments with heterogeneously distributed deformation largely coincide with lateral earthquake terminations. We therefore propose that long-lived plate interface deformation promotes stress build-up and leads to earthquake nucleation. Earthquakes then propagate along fault planes shielded from this long-lived permanent deformation, and are finally stopped by segments of heterogeneously distributed deformation. Slip deficit patterns and earthquake segmentation therefore reflect the along-dip and along-strike distribution of the plate interface deformation. Topography acts as a mirror of distributed plate interface deformation and should be ~~studied systematically~~ systematically studied to improve the prediction of earthquake ruptures.

1 Introduction

Predicting the extent of subduction zone seismic ruptures mostly relies on geodetic observations of interseismic coupling (e.g., Moreno et al., 2010), notwithstanding spatial resolution issues (Loveless and Meade, 2011). Some earthquakes have however ruptured low coupled zones (Noda and Lapusta, 2013) or only part of highly locked patches (e.g., Konca et al., 2008). This was the case for the 2014 Mw 8.4 Iquique earthquake, which only ruptured the northern end of the North Chile gap (last broken in

25 1877, Ruiz et al., 2014a), or the Tocopilla Mw 7.8 earthquake, which struck the down-dip and less coupled part of the same gap seven years before (Delouis et al., 1998; Metois et al., 2016) (Fig. 1). Predicting the location and extent of earthquakes clearly requires a better understanding of earthquake mechanics.

Subduction earthquake propagation has so far been either related to megathrust frictional ~~properties (Perfettini et al., 2010; Kaneko et al.,~~ pore fluid pressure properties (Perfettini et al., 2010; Kaneko et al., 2010; Moreno et al., 2014) , inherited stress states (Konca

30 et al., 2008; Kaneko et al., 2010) or seafloor roughness ~~(Kodaira et al., 2000; Wang and Bilek, 2014)~~ (Kodaira et al., 2000; Wang and Bilek, Megathrusts, commonly regarded as interfingered seismic and aseismic patches with contrasting frictional properties, are conventionally sub-divided into four domains with depth (A-D, Lay et al., 2012). The highly coupled domain-B hosts megaearthquakes, while the partly coupled domain-C is characterized by moderate slip earthquakes generating significant high frequency seismic radiation (Lay et al., 2012).

35 The distribution of these patches might persist over time scales up to ~~the~~ million years and control forearc morphology (Song and Simons, 2003). A spatial correlation between the coastline and the down-dip limit of the strongly locked zone has indeed been evidenced along the northern chilean margin (Béjar-Pizarro et al., 2013; Metois et al., 2016). Coastal uplift rates inferred from marine terraces, between 0.1 and 0.3 mm/a over the last 400 ka (Saillard et al., 2017), have been linked to the change of mechanical coupling between domains B and C (Saillard et al., 2017) or to underplating (Delouis et al., 1998; Adam

40 and Reuther, 2000; Clift and Hartley, 2007). Numerical investigations recently suggested that underplating, through transient stripping of the slab-top near the base of the forearc crust, may generate periodic Myr-long uplift sequences and a trackable 100 m-high topographic signal (Menant et al., 2020).

Bathymetric features are considered as potential seismic barriers, based on the distribution of incoming plate roughness (Wang and Bilek, 2014; Lallemand et al., 2018) or gravimetric anomalies (Bassett and Watts, 2015). Subduction of bathymetric

45 features induces large fracture networks, promoting removal of material from the bottom of the overriding plate (basal erosion, Ranero and von Huene, 2000) and potentially characteristic topographic features (Dominguez et al., 1998; Collot et al., 2008; Ruh et al., 2016). Hetereogeneities in the structure of the damaged plate interface and stress field, as a result, would favor aseismic slip and impede the propagation of large ruptures (Wang and Bilek, 2014). Very few seismic surveys, however, have imaged seamounts surrounding a large rupture (Kodaira et al., 2000; Geersen et al., 2015).

50 We herein explore an alternative explanation: rather than variations of frictional properties or of seafloor roughness, earthquake segmentation might relate to the distribution of deformation along the plate interface (Wang and Bilek, 2014), as observed along strike-slip faults (Wesnousky, 2006). Both underplating and basal erosion require the redistribution of deformation ultimately leading to the migration of the plate boundary (Vannucchi et al., 2012; Agard et al., 2018). We here show that the location of such distributed deformation along the plate interface can be captured from a simple mechanical analysis of the topog-

55 raphy, since underplating and basal erosion both impact forearc morphology. This method is applied over a 2000km long strech along the Chilean margin, known to transition from erosive to accretionary from north to south, as incoming sediment thickness increases ~~(Clift and Vannucchi, 2004; Clift and Hartley, 2007)~~ (von Huene and Ranero, 2003; Clift and Vannucchi, 2004; Clift and Hartley 1a). This margin is one of the best instrumented subduction zones, along which five mega-earthquakes, including a domain-C event, have occurred during the last 25 years (Fig. 1c). We first map out the location of distributed deformation zones associ-

60 ated with basal erosion and underplating and compare them with the megathrust segmentation proposed so far. We then discuss how distributed deformation along the plate interface impacts and therefore can be used to constrain earthquake extent and mechanics.

2 Methodology

~~To do so, we~~ We applied the critical taper theory ~~(CTT, Davis et al., 1983, Fig. 2a)~~ (CTT, Davis et al., 1983, Fig. 2) . The the-
65 ory predicts the topographic slope of a wedge on the verge of failure as well as dips of its internal faults, from the frictional and pore fluid pressure properties of the wedge and megathrust (Dahlen, 1984). We used the solution of Dahlen (1984) for a non cohesive wedge, describing the critical taper, formed by the topographic slope α and the slab dip β, as a function of the angle Ψ_B formed by the maximum principal stress σ_1 and the base of the wedge and the angle Ψ_0 formed by σ_1 and the top of the wedge. The solution for the lower compressional branch is:

70
$$(\alpha + \beta)_c = \Psi_B - \Psi_0 \tag{1}$$

with

$$\Psi_B = \frac{1}{2} arcsin(\frac{sin\phi_b'}{sin\phi_b}) - \frac{1}{2}\phi_b' , \tag{2}$$

$$\Psi_0 = \frac{1}{2} arcsin(\frac{sin\alpha'}{sin\phi_{int}}) - \frac{1}{2}\alpha'. \tag{3}$$

75 The angles ϕ_{int} and ϕ_b are the internal and basal coefficients of friction defined as $\mu_{int} = tan\phi_{int}$ and $\mu_b = tan\phi_b$, and

$$\phi_b' = arctan\left[\left(\frac{1-\lambda_b}{1-\lambda}\right)tan\phi_b\right] , \tag{4}$$

$$\alpha' = arctan\left[\left(\frac{1-\rho_w/\rho}{1-\lambda}\right)tan\alpha\right] . \tag{5}$$

The internal and basal Hubbert-Rubbey fluid pressure ratios λ and λ_b are defined in (Davis et al., 1983) as:

80
$$\lambda = \frac{P - \rho_w gD}{|\sigma_z| - \rho_w gD} , \tag{6}$$

$$\lambda_b = \frac{P_b - \rho_w gD}{|\sigma_z| - \rho_w gD} , \tag{7}$$

where ρ and ρ_w are the wedge material and water densities and D is the water depth. The solution is exact if $\lambda = \lambda_b$ and the approximation is valid for small tapers as used in this study (Wang et al., 2006).

3

The relationship between the topographic slope α and the slab dip β forms an envelope separating different mechanical states (Fig. 2a). The wedge is at critical state if the taper formed by α and β follows a critical envelope. In that case, activation of the megathrust requires internal faulting. In contrast, if the taper exceeds this critical limit, the wedge enters in a stable domain (in the sense of the CTT), where the only possible active fault is the megathrust.

Dynamic effective frictions of seismogenic zones have been shown to reach extremely low values ($\mu \sim 0.01 - 0.03$, Fulton et al., 2013; Gao and Wang, 2014). As a consequence, a forearc above a seismogenic megathrust, with standard α and β, will systematically fall in the CTT stable domain (Fig. 2a). In contrast, aseismic megathrusts are characterized by larger effective friction ($\mu \sim 0.1 - 0.15$, Cubas et al., 2013; Gao and Wang, 2014), allowing the wedge to reach critical conditions (Cubas et al., 2013) (Fig. 2a). Furthermore, at critical state, if the basal effective friction of the wedge approaches the internal effective friction, the dip of internal faults within the wedge will decrease and become parallel to the plate interface. A small difference of friction will thus lead to deformation either by basal accretion (in the lower plate) or by basal erosion (in the upper plate), instead of standard accretion characterized by thrust faults reaching the surface (Dahlen, 1984) (Fig. 2a). If the basal effective friction reaches the internal one, a highly fractured forearc is even expected.

Following the method of (Cubas et al., 2013) , we

We here used inversion to retrieve the effective basal friction, the internal friction and internal pore pressure ratio from the $\alpha - \beta$ co-variation. To do so, we followed the procedure developed by Cubas et al. (2013) and detailed in Supplementary Materials. We used ETOPO 1 for (Amante and Eakins, 2009) to derive the bathymetric and topographic slope, and slab 2.0 (Hayes et al., 2018) for the slab dip(Hayes et al., 2018) . We built swath profiles perpendicular to the trench every 0.1 longitudinal degree (Suppl. Mat. Fig. 1), smoothed by a rectangular window, degree along trench to get average topographic slopes and slab dips with their standard deviations necessary to the inversion procedure (Fig. 2, Suppl. Mat. Fig. 2, 5). Along these S1). We explored from 10 to 45° for ϕ_{int}, from 1 to 44.9^o for ϕ_b^{eff}, and from 0.35 to 0.975 for λ. Along the $\alpha - \beta$ profiles, we selected segments parallel to critical envelops . with a slope comprised between the two extreme theoretical envelops of the parameter set (Fig. 3, Suppl. Mat. Fig. S2). For each of these segments, we retrieved , by inversion, probability density functions for the friction of the wedge, the pore pressure ratio of the wedge and the effective friction of the megathrust (Suppl. Mat. Fig. 3) . The CTT inversion only provides the internal pore pressure, which can be considered as a lower bound for the megathrust pore pressure. Moreover, close effective internal and basal frictions implies close internal and megathrust pore pressure. The inversion procedure is described in (Cubas et al., 2013) . S3) and best misfit sets (Suppl. Mat. Fig. S4). We only kept segments with extremely low misfits misfits lower than 0.1, and with values consistent with standard frictions(: from 25 to 43° for ϕ_{int} , Byerlee (1978) , (consistent with lab experiment values (Byerlee, 1978)), from 1 to 42.9^o for ϕ_b^{eff} (same range as the internal friction but considering additional pore fluid pressure effect), and from 0.35 to 0. 95 975 for λ). Sensitivity tests were run by Cubas et al. (2013) , showing that an error of $\pm 5^o$ on β implies a horizontal translation of the taper and a 3° variation for the effective basal friction, without affecting the critical state of the forearc. Best misfits for each parameter are provided in Supplementary Material (Table 1 Fig. 6) . Figure 3a-c shows the fit between the $\alpha - \beta$ profiles and the envelops corresponding to the best misfit of the identified critical segments. These segments (Fig. 3b-d) have then been reported on Fig. 1b.

3 Results

3.1 Locating plate interface deformation

Since we seek to capture distribution of deformation along the plate interface, we compared the internal and megathrust effective frictions and mapped the difference (Fig. 1b). A one degree difference implies a dip difference $< 10^o$ between the megathrust and the forward-verging thrusts. This representation allows inferring areas prone to either standard accretion, or to basal erosion/accretion, the latter being herein defined as distributed deformation along the plate interface.

The transition from erosion to accretion is particularly well captured by the method despite its relative simplicity (Fig. 1a-b). North of ~~25°~~26°S (i.e., at the transition between erosive and accretionary subduction), the difference of effective frictions is systematically lower than 2°, and mostly lower than 1°, which means that deformation is essentially located along the plate interface. The difference increases notably south of the Juan Fernandez ~~ridge~~Ridge, and progresses inland towards the south, consistent with active faults mapped near the Arauco peninsula (Fig. 1d). The method also captures basal erosion linked to the few subducted seamounts imaged around the Iquique rupture (Geersen et al., 2015) (Fig. 1c).

To interpret the origin of plate interface deformation, we set the limit between accretion and interface deformation for a difference of friction angle of one degree and then searched for the depth distribution of each process (Fig. 4a-b). Results for different thresholds are also presented.

Accretion mostly occurs at depths shallower than 20 km whereas distributed deformation along the plate interface is found at every depth with three favorable peaks: a first one at 15 km depth, a second at 35±10 km depth and a third at 60±5 km depth. Basal erosion due to bathymetric features is known to be efficient at shallow depth (von Huene et al., 2004), but might also occur slightly deeper as testified by subsidence of forearc basins (Clift and Hartley, 2007). Underplating has been observed at shallow depth (Kimura et al., 2010; Tréhu et al., 2019; Bangs et al., 2020), even for seamount moats (Clarke et al., 2018), but mostly occurs below 30-40 km, i.e. the long-term coupling-decoupling transition (Agard et al., 2018). The compilation of P-T conditions for recovered underplated material shows a similar distribution as CTT, with peaks at depths of 30±5 km and 50±5 km and a gap in between (Fig. 4b). Numerical modelling also suggests that erosion predominates over underplating at depths shallower than 20 km (Menant et al., 2020). As a consequence, we assume that the interface deformation documented here mostly relates to basal erosion for depths < 20 km, whereas underplating dominates at greater depths, in particular below the coast.

This depth divide between basal erosion and underplating is strengthened by estimates of pore fluid pressure ratio (Fig. 4d-f). If low pore fluid pressure is mainly found in accretion conditions, higher fluid pressure dominates where basal erosion occurs (von Huene and Ranero, 2003; Vannucchi et al., 2012). On the contrary, recovered underplated material from greater depth present very consistent P-T conditions of lithostatic pressure, which rules out any significant fluid overpressure (Agard et al., 2018). The first peak for basal erosion at low pore fluid pressures in Fig. 4e could be related to the 20 km depth assumption and

reveal the minor occurrence of underplating at shallower depth. The trimodal distribution deduced from CCT (one peak for basal erosion and two peaks for underplating) and differences in pore pressure remains for a 0.5^o or a 2° difference of friction.

Most of the critical segments attesting to distributed interface deformation have lengths smaller than 7 km, and do not exceed 20 km (Fig. 4c). This is in good agreement with the length of graben and horst and seamounts observed on the subducting plate (von Huene and Ranero, 2003; Geersen et al., 2015). This is also consistent with seismic observations (Kimura et al., 2010; Tréhu et al., 2019; Bangs et al., 2020) and the long-term rock record showing generally $\leq$ 300-500 m thick exhumed slices from the top of the slab (Agard et al., 2018) extending 5-10 km downdip at most (Plunder et al., 2012, 2013). Such tabular shape ratios, with seamounts probably near the higher bound (Bonnet et al., 2019), further support interface deformation parallel to the megathrust (Fagereng and Sibson, 2010; Rowe et al., 2013).

3.2 Relating plate interface deformation with long-term coastal uplift

In order to approach internal effective friction, the basal friction of the wedge needs to be relatively high (Fig. 2a). Deformation captured at depth by CTT therefore corresponds to underplating in the making, when deformation is still distributed: once tectonic slicing is achieved, basal friction will reach low values characteristic of mature faults, bringing the taper in the stable domain and impeding detection by CTT.

We here show that active, incipient underplating takes place along most of the Chilean margin (Fig. 1, 5a), whether or not strain accumulation ultimately turns these critical zones into tectonic slices (Agard et al., 2018; Bonnet et al., 2019; Kimura et al., 2007). Along the Tocopilla and Maule segments, incipient underplating takes place below the slab - continental Moho intercept (orange curve on Fig. 1c), whereas it is located above and near the intercept between 25-33°S. Along the northern erosive margin (Fig. 5a-b), the thin oceanic sediment cover together with eroded material and possibly pieces stripped from the subducting plate are being underplated. Southward, larger sediment input favors shallow accretion and underplating of subducted sediments (Fig. 5a-b), as locally observed by seismic surveys (Tréhu et al., 2019).

To evaluate the possible link between coastal uplift and regions of distributed deformation along the plate interface, we compare our spatial distribution of underplating with documented marine terraces and uplift rates (Saillard et al., 2017) (Fig. 5a-c). While the irregular distribution of marine terraces may relate to fragmentary preservation rather than discontinuous underplating, most of them coincide with segments of underplating (or with standard accretion near the Arauco peninsula). The typical length of the segments showing distributed deformation along the interface is modest ($\sim$10-20 km). This advocates for propagation of deformation only into the topmost part of the subducting plate, e.g. into the stack of oceanic/eroded material or along a hydrated basalt layer within the crust. Although the comparison with uplift rates inferred from morphometric analysis and modelling of landscape evolution (Melnick, 2016) shows no particular pattern, underplating of relatively thin slices would be consistent with both the low uplift rates and the rock record (Agard et al., 2018).

Shallow normal faults identified along northern Chile have been related to potential underplating (Adam and Reuther, 2000; Clift and Hartley, 2007). We here show that they are located above underplating areas, and that normal faults transition southward to thrusts where accretion prevails (Fig. 5a-c).

3.3 Large megathrust earthquakes are surrounded by plate interface deformation

We now compare zones of distributed deformation with areas struck by recent large earthquakes (Fig. 1c). The Mw 8.1 2014 Iquique earthquake is surrounded by patches of distributed deformation associated with basal erosion according to their depth and to seamounts detected in the area (Geersen et al., 2015). The aftershock, located 50 km south of the main event, also falls in between patches of distributed deformation. The Mw 7.8 2007 Tocopilla earthquake is limited up-dip as well as to the south by interface deformation attributed to underplating. The Mw 8.1 1995 Antofagasta earthquake seems limited up- and down-dip by distributed deformation along the plate interface. The high slip ~~patch~~ areas of the Mw 8.2 2015 Illapel and the Mw 8.7 2010 Maule earthquakes are both limited down-dip by plate interface deformation. Their frontal extent partially propagates in areas at critical state but corresponding to standard accretion. A small portion of the ~~areas of limited slip overlaps the distributed deformationpatches. However~~earthquake ruptures do overlap with the plate interface deformation, but high slip areas are always clearly limited by plate interface deformation. Moreover, Fig. 6 shows the diversity of published co-seismic models, emphasizing the uncertainties related to the proposed slip areas, that need to be taken into account for the comparison.

To summarize, along the accretionary part of the margin, mega-earthquakes are delimited down-dip by underplating whereas along the erosive domain, the extent is controlled by both basal erosion ~~, at rather shallow depth,~~ and underplating.

We now investigate the relationships between the critical segments characterized by relatively high effective basal friction, hence expected to behave aseismically, both with the along-strike segmentation inferred for large historical earthquakes (Mw $\geq$ 7.5, Saillard et al., 2017, Fig. 5a-d) and with the estimates of coupling (Metois et al., 2016; Klein et al., 2018, Fig. 5a-e). Segments with limited ~~underplating~~ plate interface deformation ($<$15 km) coincide with a significant number of rupture terminations (blue and grey overlays, respectively: Fig. 5a-d), particularly in the southern region. ~~The distribution of underplating also shows~~ Between 29 and 24°S, rupture terminations coincide with segments where plate interface deformation is reduced. The underplating segments also show a long wavelength distribution (4 to 8° degrees latitude) corresponding to the three main seismic ~~domains~~ regions visible on Fig. 5a,d (respectively located north of Mejillones, between Mejillones and Punta Choros, and to the south of Punta Choros). No correlation exists with sediment input (Fig. 5b). ~~Marine terraces are mostly found where underplating is maximum, i.e. in the central domain (Fig. 5c).~~ The proportion of a swath profile at critical state is then compared to the average estimate of coupling along this profile (Fig. 5e). A positive correlation is evidenced at small scale (1.5 and 2 ^{o} degrees latitude, Suppl. Mat. S7) between the segments with minimal underplating (blue overlays; Fig. 5a) and the regions of minimal coupling (red overlays; Fig. 5e). On a larger scale (4 and 8° degrees latitude, Suppl. Mat. fig.7), an anti-correlation is observed with coupling: zones of high coupling correspond to domains where underplating is somewhat more limited (e.g., between 31 and 38°S). As shown by Fig. 1d, areas marked by intense plate deformation are mostly located down-dip of the highly locked patches, in particular in the south. Continuous and voluminous sediment influx provides spatially and temporally stable mechanical conditions (Olsen et al., 2020). This leads to stationary seismic asperities followed, once the Moho is crossed, by the regular underplating of very thin and relatively short slices (typically 300-500 m thick, 5-10 km long). This spatial and temporal stability promotes topographic build-up, explaining the spatial coincidence between strongly coupled patches and efficient underplating. In contrast, segments with limited underplating might reveal spatially and temporally heterogeneous

conditions along the megathrust (Olsen et al., 2020), i.e. heterogeneous deformation impeding earthquake propagation and significant topographic build-up.

Noteworthily, the hypocenters of the last major events lie at the boundary with a patch of distributed deformation. Finally, we show that the high frequency radiations generated by Maule and Illapel earthquakes (Wang and Mori, 2011; Meng et al., 2015, 2018) coincide with areas of extensive interplate deformation (Fig. 1c), along which spatially restricted fault planes might have been dynamically triggered.

4   Discussion ~~- Conclusion~~

4.1   Link between earthquake ruptures and plate interface deformation

We herein show two major results: (1) recent earthquakes are bounded by extensive plate interface deformation characterized, along the southern accretionary part of the margin by underplating at their down-dip edge and, along the northern erosive part of the margin by both basal erosion and underplating (Fig. 1); (2) along strike, segments characterized by minimal interplate deformation largely coincide with lateral earthquake terminations (circles; Fig. 5d). These observations demonstrate a close link between distributed interplate deformation and earthquake segmentation.

We therefore propose that plastic deformation and stress build-up associated with interplate deformation along distributed fault planes of limited extent (Fig. 7 - step 1) ~~,~~ eventually leads to mega-earthquake nucleation (Fig. 7 - step 2). This ~~process may be accompanied by transient seismic/slip events hardly resolvable by geodetic means due to their size, depth or distance to the coast, as expected in zones of distributed deformation and of high pore fluid pressure (Liu and Rice, 2007; Kimura et al., 2010; Collot et al., This~~ is suggested by the location of hypocenters at boundaries with distributed deformation (Fig. 1)~~and .~~ This interseismic deformation might be accompanied by some micro-seismicity, as observed prior to the Iquique rupture (Schurr et al., 2020) and in the upper plate in northern Chile (Sippl et al., 2018) . If high pore fluid pressure prevails, this deformation could also be accompanied by transient seismic/slip events (Liu and Rice, 2007; Kimura et al., 2010; Collot et al., 2017) , which concords with observations for the Iquique earthquake (Ruiz et al., 2014a; Meng et al., 2015; Socquet et al., 2017) and others elsewhere ~~(Tohoku, Kato et al., 2012) , (Guerrero, Radiguet et al., 2016) .~~ (Tohoku, Kato et al. (2012) ; Guerrero, Radiguet et al. (2016)).

Once nucleated, large earthquakes propagate along well localized and smoothed rate-weakening fault planes (Bletery et al., 2016) ~~bounded~~ limited by elongate zones of underplating ~~(or basal erosion when present;~~ which, in addition, inhibit further rupture propagation and slip (Fig. 1, 7 - step 3).

These earthquakes abut on regions of heterogeneously distributed deformation and stress concentrations (Fig. 7 - step 4), ~~which inhibit~~ impeding the development of well localized slip zones (Wang and Bilek, 2014)~~and impede rupture propagation~~ , and again significant slip (Wesnousky, 2006). Some of these fractures might however slip seismically during large events and produce the observed high frequency radiations (Meng et al., 2018, 2015).

4.2 Down-dip segmentation and plate interface deformation

Within this framework, domain-C (Lay et al., 2012) would correspond to the region of incipient underplating, and domain-B to the smoothed rate-weakening fault zone. This is consistent with partial coupling of domain-C, where deformation is dominated by creep mechanisms, and elastic strain is accumulated along undeformed segments of the megathrust, producing moderate slip earthquakes with a higher recurrence time and significant coherent short-period seismic radiations. Domain-C might more specifically be delimited by the two underplating peaks (Fig. 4), the upper one corresponding to the slicing of oceanic sediments and/or eroded continental material, the second to the propagation of deformation into the hydrated basalt layer once the continental Moho is crossed (Agard et al., 2018), a process ultimately leading to the underplating of very thin and relatively short slices (typically 300-500 m thick, 5-10 km long, Agard et al., 2018).

Data suggest that domain-C, by locally concentrating interplate permanent deformation due to specific geometry (i.e., morphological asperities) and/or mechanical behaviour (i.e., frictional properties, fluid content, porosity), shields the rate-weakening domain-B from long-lived deformation (Fig. 7). Contrary to the prevalent paradigm, domain-B should not be regarded as an 'asperity', i.e. a strongly coupled yet mechanically weak zone with high recurrence time earthquakes, but instead as a relatively weak zone devoid of permanent deformation and only storing elastic energy. In this new paradigm, loading along domain-C tightly controls slip deficit as well as rupture nucleation and extent along domain-B (Fig. 7), explaining the correlation observed between historical earthquakes, earthquake terminations and distributed plate interface deformation (Fig. 5 a,d). On the short-term scale, elastic deformation generates subsidence at the coast during domain-B earthquakes and uplift for domain-C events (Melnick, 2016). On the long-term, the thin underplated slices ultimately build a Myr topographic signal of slow uplift, particularly difficult to capture with geodetic measurements due to the interplay of elastic and plastic deformation (Menant et al., 2020). The Coastal Cordillera present along much of the Chilean margin could result from this long-term underplating process. The absence of upper plate deformation above the seismogenic zone in conjunction with topographic build-up above underplating areas account for the correlation between seismic behavior and gravity anomalies (Song and Simons, 2003).

5 Conclusions

We herein show, through a simple CTT analysis of topography, that, along the Chilean subduction zone, earthquakes are bounded by long-lived, extensive plate interface deformation occurring preferentially at 35 ± 10 and 60 ± 5 km depth. Along the Central Chilean margin, earthquakes are limited along their down-dip edge by underplating while, along Northern Chile, they are surrounded by distributed deformation related to both basal erosion and underplating. Plate interface deformation might control earthquake nucleation, extent and arrest, and its distribution provide a relatively ~~faithful~~ reliable image of the seismic potential at depth. This topography analysis may also remedy the lack of preserved marine terraces or weakly constrained coupling models. This method could therefore be used more systematically to identify regions with precursory transient signals and to enhance predictions of future earthquakes extent.

9

Appendix See supplementary material for detailed method and supporting figures.

Code and data availability. Data available at to be completed and code available on demand.

285 *Author contributions.* NC designed the study; NC and RT ran the simulations; NC, RT, PA analyzed the results; NC and PA wrote the paper.

Competing interests. Authors declare no competing interest.

References

Adam, J. and Reuther, C.-D.: Crustal dynamics and active fault mechanics during subduction erosion. Application of frictional wedge analysis on to the North Chilean Forearc, Tectonophysics, 321, 297–325, 2000.

Agard, P., Plunder, A., Angiboust, S., Bonnet, G., and Ruh, J.: The subduction plate interface: rock record and mechanical coupling (from long to short timescales), Lithos, 320, 537–566, 2018.

Amante, C. and Eakins, B. W.: ETOPO1 arc-minute global relief model: procedures, data sources and analysis, 2009.

Bangs, N. L., Morgan, J., Tréhu, A., Contreras-Reyes, E., Arnulf, A., Han, S., Olsen, K., and Zhang, E.: Basal accretion along the south central Chilean margin and its relationship to great earthquakes, Journal of Geophysical Research: Solid Earth, 125, e2020JB019 861, 2020.

Bassett, D. and Watts, A. B.: Gravity anomalies, crustal structure, and seismicity at subduction zones: 2. Interrelationships between fore-arc structure and seismogenic behavior, Geochemistry, Geophysics, Geosystems, 16, 1541–1576, 2015.

Béjar-Pizarro, M., Socquet, A., Armijo, R., Carrizo, D., Genrich, J., and Simons, M.: Andean structural control on interseismic coupling in the North Chile subduction zone, Nature Geoscience, 6, 462–467, 2013.

Bletery, Q., Thomas, A. M., Rempel, A. W., Karlstrom, L., Sladen, A., and De Barros, L.: Mega-earthquakes rupture flat megathrusts, Science, 354, 1027–1031, 2016.

Bonnet, G., Agard, P., Angiboust, S., Fournier, M., and Omrani, J.: No large earthquakes in fully exposed subducted seamount, Geology, 47, 407–410, 2019.

Byerlee, J.: Friction of rocks, in: Rock friction and earthquake prediction, pp. 615–626, Springer, 1978.

Chlieh, M., De Chabalier, J., Ruegg, J., Armijo, R., Dmowska, R., Campos, J., and Feigl, K.: Crustal deformation and fault slip during the seismic cycle in the North Chile subduction zone, from GPS and InSAR observations, Geophysical Journal International, 158, 695–711, 2004.

Clarke, A. P., Vannucchi, P., and Morgan, J.: Seamount chain–subduction zone interactions: Implications for accretionary and erosive subduction zone behavior, Geology, 46, 367–370, 2018.

Clift, P. and Vannucchi, P.: Controls on tectonic accretion versus erosion in subduction zones: Implications for the origin and recycling of the continental crust, Reviews of Geophysics, 42, 2004.

Clift, P. D. and Hartley, A. J.: Slow rates of subduction erosion and coastal underplating along the Andean margin of Chile and Peru, Geology, 35, 503–506, 2007.

Collot, J.-Y., Agudelo, W., Ribodetti, A., and Marcaillou, B.: Origin of a crustal splay fault and its relation to the seismogenic zone and underplating at the erosional north Ecuador–south Colombia oceanic margin, Journal of Geophysical Research: Solid Earth, 113, 2008.

Collot, J.-Y., Sanclemente, E., Nocquet, J.-M., Leprêtre, A., Ribodetti, A., Jarrin, P., Chlieh, M., Graindorge, D., and Charvis, P.: Subducted oceanic relief locks the shallow megathrust in central Ecuador, Journal of Geophysical Research: Solid Earth, 122, 3286–3305, 2017.

Cubas, N., Avouac, J.-P., Souloumiac, P., and Leroy, Y.: Megathrust friction determined from mechanical analysis of the forearc in the Maule earthquake area, Earth and Planetary Science Letters, 381, 92–103, 2013.

Dahlen, F.: Noncohesive critical Coulomb wedges: An exact solution, Journal of Geophysical Research: Solid Earth, 89, 10 125–10 133, 1984.

Davis, D., Suppe, J., and Dahlen, F.: Mechanics of fold-and-thrust belts and accretionary wedges, Journal of Geophysical Research: Solid Earth, 88, 1153–1172, 1983.

11

Delouis, B., Philip, H., Dorbath, L., and Cisternas, A.: Recent crustal deformation in the Antofagasta region (northern Chile) and the sub-
duction process, Geophysical Journal International, 132, 302–338, 1998.

Dominguez, S., Lallemand, S., Malavieille, J., and von Huene, R.: Upper plate deformation associated with seamount subduction, Tectono-
physics, 293, 207–224, 1998.

Duputel, Z., Jiang, J., Jolivet, R., Simons, M., Rivera, L., Ampuero, J.-P., Riel, B., Owen, S. E., Moore, A. W., Samsonov, S. V., et al.: The
Iquique earthquake sequence of April 2014: Bayesian modeling accounting for prediction uncertainty, Geophysical Research Letters, 42,
7949–7957, 2015.

Fagereng, Å. and Sibson, R. H.: Melange rheology and seismic style, Geology, 38, 751–754, 2010.

Fulton, P., Brodsky, E. E., Kano, Y., Mori, J., Chester, F., Ishikawa, T., Harris, R., Lin, W., Eguchi, N., Toczko, S., et al.: Low coseismic
friction on the Tohoku-Oki fault determined from temperature measurements, Science, 342, 1214–1217, 2013.

Gao, X. and Wang, K.: Strength of stick-slip and creeping subduction megathrusts from heat flow observations, Science, 345, 1038–1041,
2014.

Geersen, J., Ranero, C. R., Barckhausen, U., and Reichert, C.: Subducting seamounts control interplate coupling and seismic rupture in the
2014 Iquique earthquake area, Nature communications, 6, 1–6, 2015.

Hayes, G. P., Herman, M. W., Barnhart, W. D., Furlong, K. P., Riquelme, S., Benz, H. M., Bergman, E., Barrientos, S., Earle, P. S., and
Samsonov, S.: Continuing megathrust earthquake potential in Chile after the 2014 Iquique earthquake, Nature, 512, 295–298, 2014.

Hayes, G. P., Moore, G. L., Portner, D. E., Hearne, M., Flamme, H., Furtney, M., and Smoczyk, G. M.: Slab2, a comprehensive subduction
zone geometry model, Science, 362, 58–61, 2018.

Kaneko, Y., Avouac, J.-P., and Lapusta, N.: Towards inferring earthquake patterns from geodetic observations of interseismic coupling,
Nature Geoscience, 3, 363–369, 2010.

Kato, A., Obara, K., Igarashi, T., Tsuruoka, H., Nakagawa, S., and Hirata, N.: Propagation of slow slip leading up to the 2011 Mw 9.0
Tohoku-Oki earthquake, Science, 335, 705–708, 2012.

Kimura, G., Kitamura, Y., Hashimoto, Y., Yamaguchi, A., Shibata, T., Ujiie, K., and Okamoto, S.: Transition of accretionary wedge structures
around the up-dip limit of the seismogenic subduction zone, Earth and Planetary Science Letters, 255, 471–484, 2007.

Kimura, H., Takeda, T., Obara, K., and Kasahara, K.: Seismic evidence for active underplating below the megathrust earthquake zone in
Japan, Science, 329, 210–212, 2010.

Klein, E., Metois, M., Meneses, G., Vigny, C., and Delorme, A.: Bridging the gap between North and Central Chile: insight from new GPS
data on coupling complexities and the Andean sliver motion, Geophysical Journal International, 213, 1924–1933, 2018.

Kodaira, S., Takahashi, N., Nakanishi, A., Miura, S., and Kaneda, Y.: Subducted seamount imaged in the rupture zone of the 1946 Nankaido
earthquake, Science, 289, 104–106, 2000.

Konca, A. O., Avouac, J.-P., Sladen, A., Meltzner, A. J., Sieh, K., Fang, P., Li, Z., Galetzka, J., Genrich, J., Chlieh, M., et al.: Partial rupture
of a locked patch of the Sumatra megathrust during the 2007 earthquake sequence, Nature, 456, 631–635, 2008.

Lallemand, S., Peyret, M., van Rijsingen, E., Arcay, D., and Heuret, A.: Roughness Characteristics of Oceanic Seafloor Prior to Sub-
duction in Relation to the Seismogenic Potential of Subduction Zones, Geochemistry, Geophysics, Geosystems, 19, 2121–2146,
https://doi.org/10.1029/2018GC007434, 2018.

Lay, T., Kanamori, H., Ammon, C. J., Koper, K. D., Hutko, A. R., Ye, L., Yue, H., and Rushing, T. M.: Depth-varying rupture properties of
subduction zone megathrust faults, Journal of Geophysical Research: Solid Earth, 117, 2012.

Lin, Y.-n. N., Sladen, A., Ortega-Culaciati, F., Simons, M., Avouac, J.-P., Fielding, E. J., Brooks, B. A., Bevis, M., Genrich, J., Rietbrock, A., et al.: Coseismic and postseismic slip associated with the 2010 Maule Earthquake, Chile: Characterizing the Arauco Peninsula barrier effect, Journal of Geophysical Research: Solid Earth, 118, 3142–3159, 2013.

Liu, Y. and Rice, J. R.: Spontaneous and triggered aseismic deformation transients in a subduction fault model, Journal of Geophysical Research: Solid Earth, 112, 2007.

Loveless, J. P. and Meade, B. J.: Spatial correlation of interseismic coupling and coseismic rupture extent of the 2011 Mw= 9.0 Tohoku-oki earthquake, Geophysical Research Letters, 38, 2011.

Maksymowicz, A., Tréhu, A. M., Contreras-Reyes, E., and Ruiz, S.: Density-depth model of the continental wedge at the maximum slip segment of the Maule Mw8. 8 megathrust earthquake, Earth and Planetary Science Letters, 409, 265–277, 2015.

Melnick, D.: Rise of the central Andean coast by earthquakes straddling the Moho, Nature Geoscience, 9, 401–407, 2016.

Menant, A., Angiboust, S., Gerya, T., Lacassin, R., Simoes, M., and Grandin, R.: Transient stripping of subducting slabs controls periodic forearc uplift, Nature communications, 11, 1–10, 2020.

Meng, L., Huang, H., Bürgmann, R., Ampuero, J. P., and Strader, A.: Dual megathrust slip behaviors of the 2014 Iquique earthquake sequence, Earth and Planetary Science Letters, 411, 177–187, 2015.

Meng, L., Bao, H., Huang, H., Zhang, A., Bloore, A., and Liu, Z.: Double pincer movement: Encircling rupture splitting during the 2015 Mw 8.3 Illapel earthquake, Earth and Planetary Science Letters, 495, 164–173, 2018.

Metois, M., Vigny, C., and Socquet, A.: Interseismic coupling, megathrust earthquakes and seismic swarms along the Chilean subduction zone (38–18 S), Pure and Applied Geophysics, 173, 1431–1449, 2016.

Moreno, M., Rosenau, M., and Oncken, O.: 2010 Maule earthquake slip correlates with pre-seismic locking of Andean subduction zone, Nature, 467, 198–202, 2010.

Moreno, M., Haberland, C., Oncken, O., Rietbrock, A., Angiboust, S., and Heidbach, O.: Locking of the Chile subduction zone controlled by fluid pressure before the 2010 earthquake, Nature Geoscience, 7, 292–296, 2014.

Noda, H. and Lapusta, N.: Stable creeping fault segments can become destructive as a result of dynamic weakening, Nature, 493, 518, 2013.

Olsen, K. M., Bangs, N. L., Tréhu, A. M., Han, S., Arnulf, A., and Contreras-Reyes, E.: Thick, strong sediment subduction along south-central Chile and its role in great earthquakes, Earth and Planetary Science Letters, 538, 116 195, 2020.

Perfettini, H., Avouac, J.-P., Tavera, H., Kositsky, A., Nocquet, J.-M., Bondoux, F., Chlieh, M., Sladen, A., Audin, L., Farber, D. L., et al.: Seismic and aseismic slip on the Central Peru megathrust, Nature, 465, 78–81, 2010.

Plunder, A., Agard, P., Dubacq, B., Chopin, C., and Bellanger, M.: How continuous and precise is the record of P–T paths? Insights from combined thermobarometry and thermodynamic modelling into subduction dynamics (Schistes Lustrés, W. Alps), Journal of Metamorphic Geology, 30, 323–346, 2012.

Plunder, A., Agard, P., Chopin, C., and Okay, A. I.: Geodynamics of the Tavşanlı zone, western Turkey: Insights into subduction/obduction processes, Tectonophysics, 608, 884–903, 2013.

Pritchard, M. and Simons, M.: An aseismic slip pulse in northern Chile and along-strike variations in seismogenic behavior, Journal of Geophysical Research: Solid Earth, 111, 2006.

Radiguet, M., Perfettini, H., Cotte, N., Gualandi, A., Valette, B., Kostoglodov, V., Lhomme, T., Walpersdorf, A., Cano, E. C., and Campillo, M.: Triggering of the 2014 M w 7.3 Papanoa earthquake by a slow slip event in Guerrero, Mexico, Nature Geoscience, 9, 829–833, 2016.

Ranero, C. R. and von Huene, R.: Subduction erosion along the Middle America convergent margin, Nature, 404, 748–752, 2000.

Rowe, C. D., Moore, J. C., Remitti, F., and Scientists, I. E. T.: The thickness of subduction plate boundary faults from the seafloor into the seismogenic zone, Geology, 41, 991–994, 2013.

Ruh, J. B., Sallarès, V., Ranero, C. R., and Gerya, T.: Crustal deformation dynamics and stress evolution during seamount subduction: High-resolution 3-D numerical modeling, Journal of Geophysical Research: Solid Earth, 121, 6880–6902, 2016.

405 Ruiz, S., Metois, M., Fuenzalida, A., Ruiz, J., Leyton, F., Grandin, R., Vigny, C., Madariaga, R., and Campos, J.: Intense foreshocks and a slow slip event preceded the 2014 Iquique Mw 8.1 earthquake, Science, 345, 1165–1169, https://doi.org/10.1126/science.1256074, 2014a.

Ruiz, S., Metois, M., Fuenzalida, A., Ruiz, J., Leyton, F., Grandin, R., Vigny, C., Madariaga, R., and Campos, J.: Intense foreshocks and a slow slip event preceded the 2014 Iquique Mw 8.1 earthquake, Science, 345, 1165–1169, 2014b.

Saillard, M., Audin, L., Rousset, B., Avouac, J.-P., Chlieh, M., Hall, S. R., Husson, L., and Farber, D.: From the seismic cycle to long-term
410 deformation: linking seismic coupling and Quaternary coastal geomorphology along the Andean megathrust, Tectonics, 36, 241–256, 2017.

Santibáñez, I., Cembrano, J., García-Pérez, T., Costa, C., Yáñez, G., Marquardt, C., Arancibia, G., and González, G.: Crustal faults in the Chilean Andes: geological constraints and seismic potential, Andean Geology, 46, 32–65, 2018.

Schurr, B., Asch, G., Rosenau, M., Wang, R., Oncken, O., Barrientos, S., Salazar, P., and Vilotte, J.-P.: The 2007 M7. 7 Tocopilla northern
415 Chile earthquake sequence: Implications for along-strike and downdip rupture segmentation and megathrust frictional behavior, Journal of Geophysical Research: Solid Earth, 117, 2012.

Schurr, B., Moreno, M., Tréhu, A. M., Bedford, J., Kummerow, J., Li, S., and Oncken, O.: Forming a Mogi doughnut in the years prior to and immediately before the 2014 M8. 1 Iquique, northern Chile, earthquake, Geophysical Research Letters, 47, e2020GL088 351, 2020.

Sippl, C., Schurr, B., Asch, G., and Kummerow, J.: Seismicity structure of the northern Chile forearc from> 100,000 double-difference
420 relocated hypocenters, Journal of Geophysical Research: Solid Earth, 123, 4063–4087, 2018.

Socquet, A., Valdes, J. P., Jara, J., Cotton, F., Walpersdorf, A., Cotte, N., Specht, S., Ortega-Culaciati, F., Carrizo, D., and Norabuena, E.: An 8 month slow slip event triggers progressive nucleation of the 2014 Chile megathrust, Geophysical Research Letters, 44, 4046–4053, 2017.

Song, T.-R. A. and Simons, M.: Large trench-parallel gravity variations predict seismogenic behavior in subduction zones, Science, 301,
425 630–633, 2003.

Tassara, A. and Echaurren, A.: Anatomy of the Andean subduction zone: three-dimensional density model upgraded and compared against global-scale models, Geophysical Journal International, 189, 161–168, 2012.

Tilmann, F., Zhang, Y., Moreno, M., Saul, J., Eckelmann, F., Palo, M., Deng, Z., Babeyko, A., Chen, K., Baez, J., et al.: The 2015 Illapel earthquake, central Chile: A type case for a characteristic earthquake?, Geophysical Research Letters, 43, 574–583, 2016.

430 Tréhu, A. M., Hass, B., de Moor, A., Maksymowicz, A., Contreras-Reyes, E., Vera, E., and Tryon, M. D.: Geologic controls on up-dip and along-strike propagation of slip during subduction zone earthquakes from a high-resolution seismic reflection survey across the northern limit of slip during the 2010 Mw 8.8 Maule earthquake, offshore Chile, Geosphere, 15, 1751–1773, 2019.

Vannucchi, P., Sage, F., Phipps Morgan, J., Remitti, F., and Collot, J.-Y.: Toward a dynamic concept of the subduction channel at erosive convergent margins with implications for interplate material transfer, Geochemistry, Geophysics, Geosystems, 13, 2012.

435 Vigny, C., Socquet, A., Peyrat, S., Ruegg, J.-C., Métois, M., Madariaga, R., Morvan, S., Lancieri, M., Lacassin, R., Campos, J., et al.: The 2010 Mw 8.8 Maule megathrust earthquake of central Chile, monitored by GPS, Science, 332, 1417–1421, 2011.

von Huene, R. and Ranero, C. R.: Subduction erosion and basal friction along the sediment-starved convergent margin off Antofagasta, Chile, Journal of Geophysical Research: Solid Earth, 108, 2003.

14

von Huene, R., Ranero, C. R., and Vannucchi, P.: Generic model of subduction erosion, Geology, 32, 913–916, 2004.

440 Wang, D. and Mori, J.: Frequency-dependent energy radiation and fault coupling for the 2010 Mw8. 8 Maule, Chile, and 2011 Mw9. 0 Tohoku, Japan, earthquakes, Geophysical Research Letters, 38, 2011.

Wang, K. and Bilek, S. L.: Invited review paper: Fault creep caused by subduction of rough seafloor relief, Tectonophysics, 610, 1–24, 2014.

Wang, K., He, J., and Hu, Y.: A note on pore fluid pressure ratios in the Coulomb wedge theory, Geophysical research letters, 33, 2006.

Wesnousky, S. G.: Predicting the endpoints of earthquake ruptures, Nature, 444, 358–360, 2006.
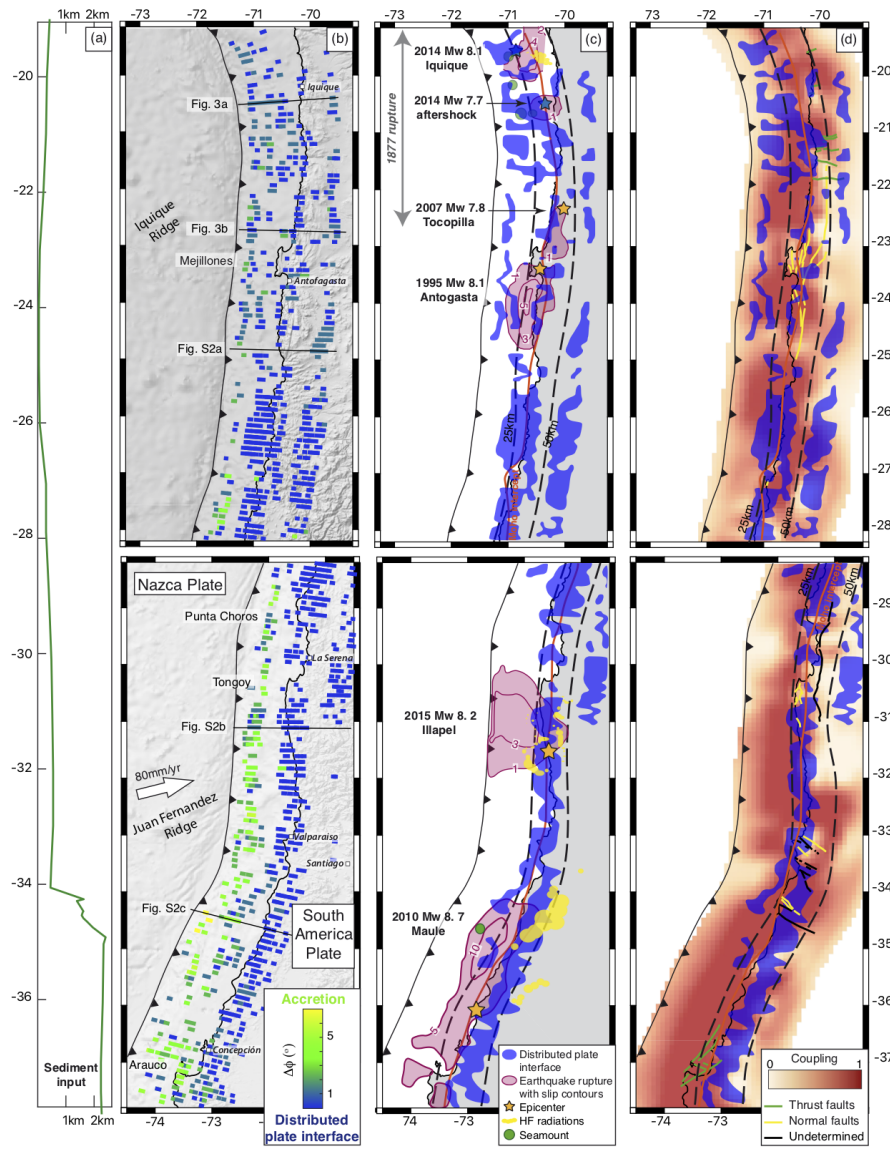
Figure 1. (a) Sediment thickness at trench (Santibáñez et al., 2018; Tréhu et al., 2019) . (b) Difference between internal and basal effective frictions of identified critical segments. Large differences lead to standard accretion with thrust faults reaching the surface, while small differences lead to the development of faults parallel to the plate interface allowing for either basal erosion or underplating. (c) Interpreted patches with distributed deformation along the plate interface related to either basal erosion or underplating compared to last major events (Maule slip contours every 2.5m (Lin et al., 2013) ; Iquique 2014 (Ruiz et al., 2014b) , Illapel 2015 (Tilmann et al., 2016) , and Antofagasta 1995 (Chlieh et al., 2004) from 1m every meter; Tocopilla 2007 (Béjar-Pizarro et al., 2013) and aftershock of Iquique 2014 0.5m slip contours (Ruiz et al., 2014b)). Orange stars: gCMT solutions, blue stars: CSN catalog. High frequencies radiations (yellow, Wang and Mori, 2011; Meng et al., 2015, 2018) , identified seamounts (green, Geersen et al., 2015; Maksymowicz et al., 2015) , slab depths (dashed black, Hayes et al., 2018) and slab-Moho intercept (orange, Tassara and Echaurren, 2012) . (d) Interpreted patches with distributed plate interface compared to coupling model (Metois et al., 2016) with known active faults (Santibáñez et al., 2018) .

Figure 1. (a) Sediment thickness at trench (Santibáñez et al., 2018; Tréhu et al., 2019) . (b) Difference between internal and basal effective frictions of identified critical segments. Large differences lead to standard accretion with thrust faults reaching the surface, while small differences lead to the development of faults parallel to the plate interface allowing for either basal erosion
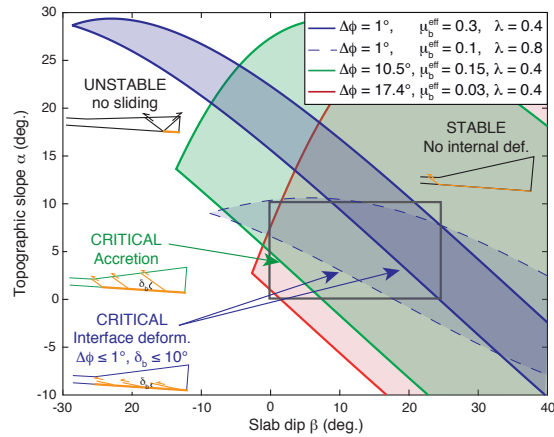
16

Figure 2. ~~(a)~~ Critical taper theory with different mechanical states. The grey rectangle represents the standard range of topographic slope α and slab dip β of subduction zones. With extremely low effective friction along the megathrust (red curve), the wedge systematically falls in the stable domain. With larger effective friction, and large difference of effective friction between the megathrust and the wedge (green curve), the wedge can reach the accretionary critical state characterized by internal faulting. With a reduced difference (blue curves), a wedge can still reach the critical state but the dip of internal faults within the wedge will decrease and become parallel to the plate interface. High pore fluid pressure facilitates interface deformation for low slab dips (dashed blue curve), whereas lower pore fluid pressure induces interface deformation at larger slab dip (plain blue curve). ~~(b) Topographic slope (α) versus slab dip (β) for a swath profile along the Iquique segment and (c) along the Tocopilla segment (locations on Fig. 1b and Suppl. Mat. fig. 1). Segments at critical state, according to inversion, are shown in blue: light blue when probably erosive, dark blue for probable underplating. Grey: swath plus or minus standard deviation. Properties of each segment are provided in Suppl. Mat. table 1.~~
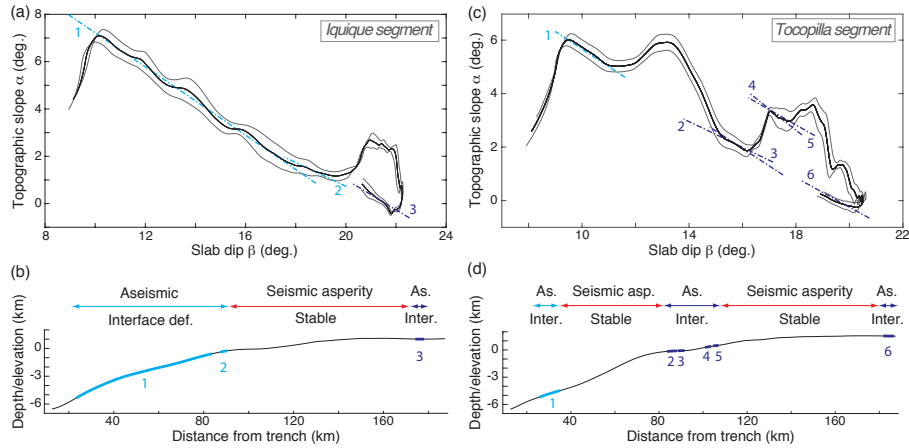
Figure 3. (a) Topographic slope (α) versus slab dip (β) for a swath profile along the Iquique segment (locations on Fig. 1b). Grey: swath plus or minus standard deviation. Segments at critical state, according to inversion, are shown in blue. For every segment, the difference between the effective internal and basal frictions is lower than 1 (properties of each segment are provided in Suppl. Mat. table 1). They are thus interpreted as regions of favorable plate interface deformation, shown in light blue when probably erosive, dark blue for probable underplating. Depth and distance to the trench can be appreciated in Suppl. Mat. Fig. S5. (b) Relocation of the critical segments on the swath profile. (c) Topographic slope (α) versus slab dip (β) and (d) Relocation of the critical segments for a swath profile along the Tocopilla segment.
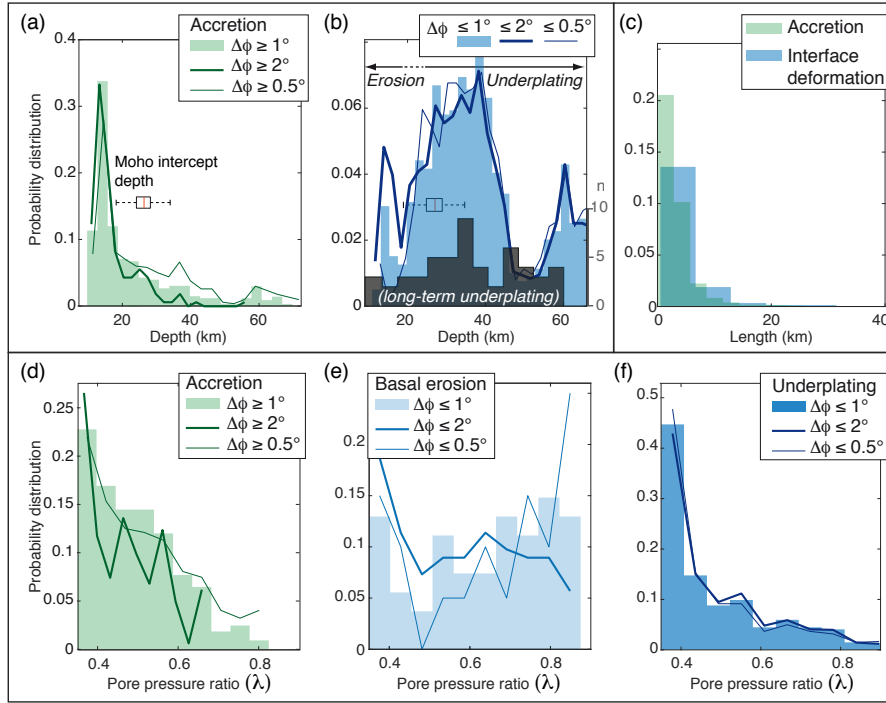
Figure 4. (a) Mean depth of segments at accretionary critical state and (b) distributed plate interface deformation critical state, compared to a compilation of the maximum burial depth reached by exhumed tectonic slicing (grey, Agard et al., 2018), and to the box plot of the Moho intercept depth (Tassara and Echaurren, 2012) . (c) Length of segments at accretionary and distributed plate interface deformation critical state. (d), (e) and (f) Pore fluid ratio λ of segments at accretionary, basal erosion or underplating critical state, assuming that basal erosion prevails above 20 km depth, and underplating below. ~~Histograms~~ Histogram curves are shown for a 1° difference of internal and basal effective friction, thin line for a 0.5^o difference, bold line for 2° (curves were chosen for sake of clarity).
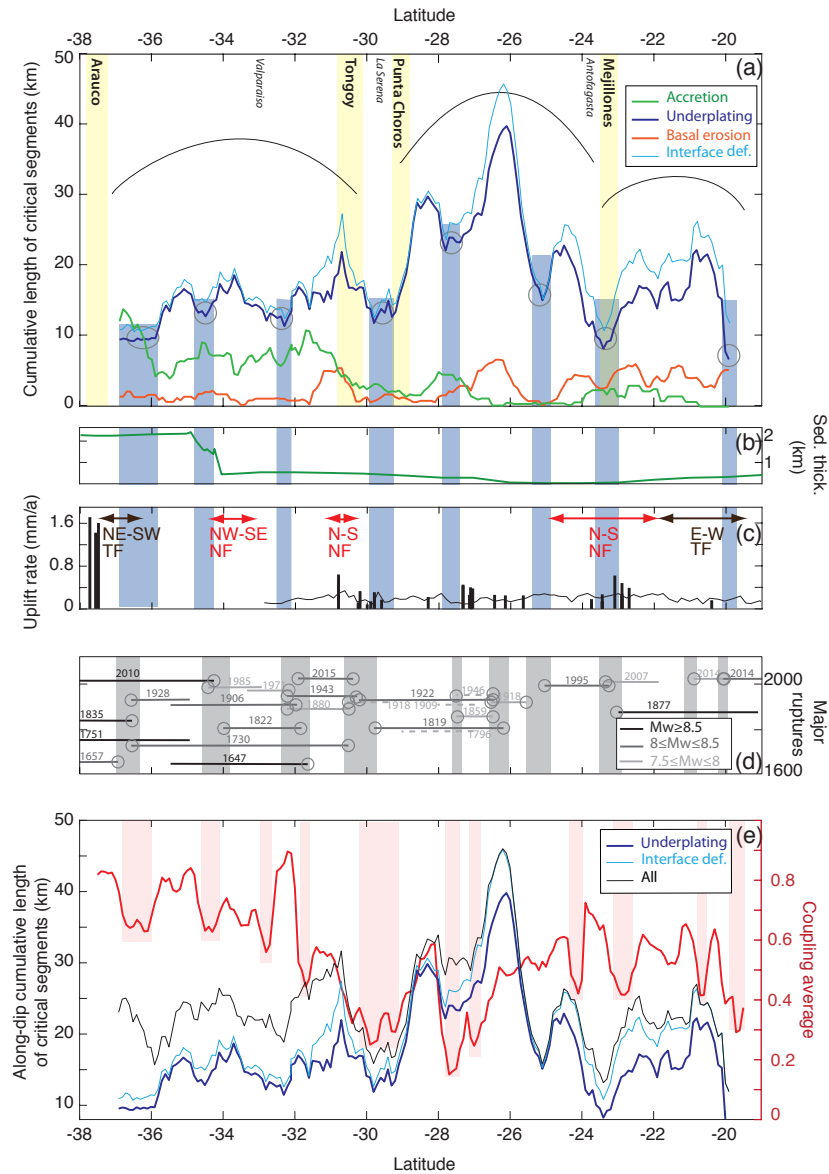
Figure 5. (a) Along-dip cumulative length of segments at accretionary (green), underplating (dark blue) or basal erosion (orange) critical state (length smoothed by a rectangular window over 8 profiles). The light blue curve shows the cumulative length of segments with interface deformation (basal erosion + underplating). Regions with limited underplating (and interface deformation) length are represented by blue bands. (b) Thickness of sediment income (green, Santibáñez et al., 2018; Tréhu et al., 2019). (c) Quaternary uplift rates of marine terraces (black bars, largest average rate since terrace abandonment, Saillard et al., 2017), coastal uplift rate obtained from a landscape evolution model (black curve, Melnick, 2016) and extent of known active faults (NF: normal fault, TF: thrust fault, Santibáñez et al., 2018). (d) Along-strike extent of historical megathrust ruptures (Saillard et al., 2017). (e) Comparison between the cumulative length of segments at critical state (thin black), with underplating (thick blue), with both underplating and basal erosion (light blue) and the average coupling value along profiles from Metois et al. (2016) corrected by Klein et al. (2018) between 24.5^oS and 28^oS (plain red curve). Red bands show segments of decreasing coupling. Correlation factor between coupling and underplating: $r = -0.36$, between coupling and underplating + basal erosion: $r = -0.39$.
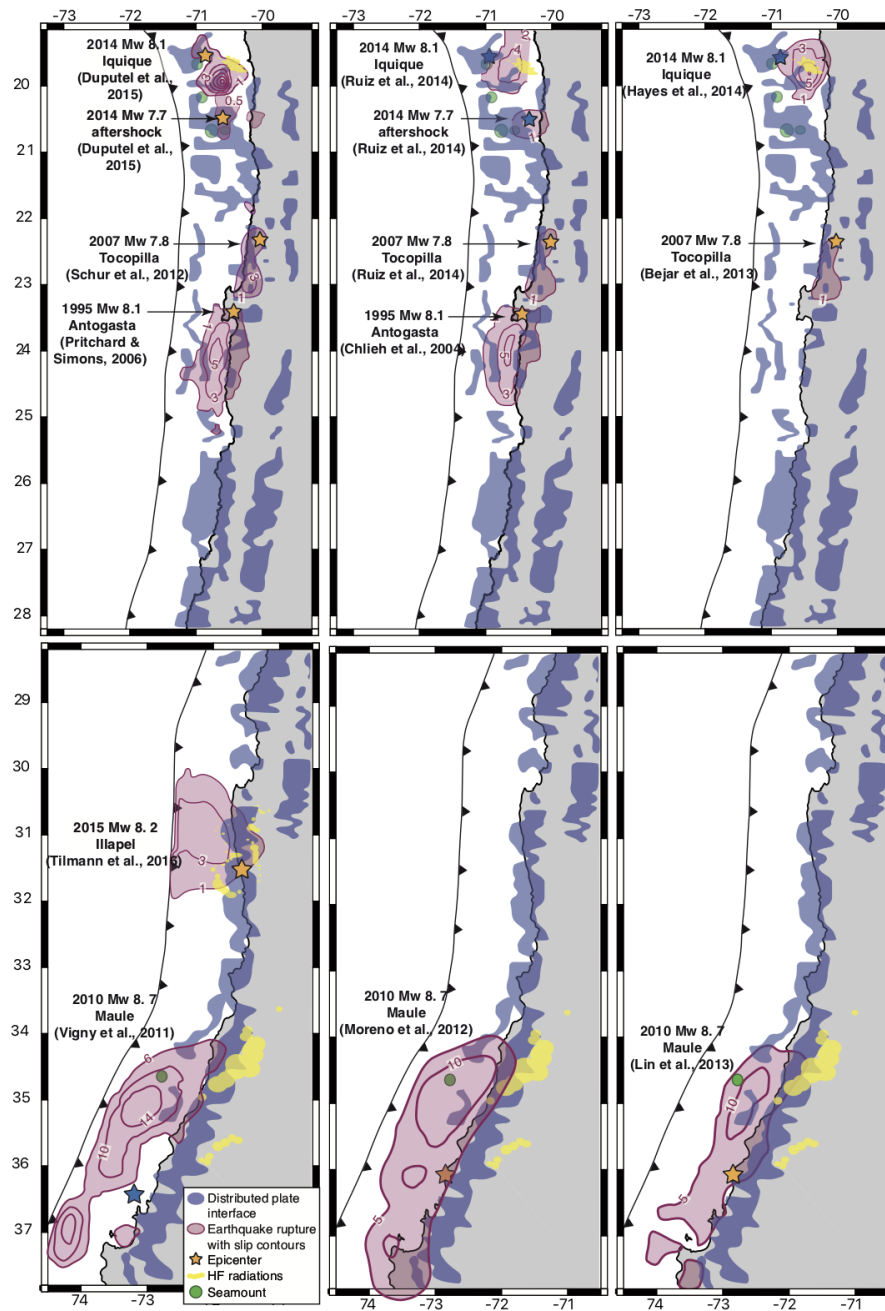
Figure 6. Areas prone to distributed deformation along the plate interface compared to various published co-seismic slip models (Duputel et al., 2015; Schurr et al., 2012; Pritchard and Simons, 2006; Tilmann et al., 2016; Vigny et al., 2011; Ruiz et al., 2014b; Chlieh et al., 2004; Moreno et al., 2010; Hayes et al., 2014; Béjar-Pizarro et al., 2013; Lin et al., 2013). Orange stars: gCMT solution, blue stars: CSN solution.
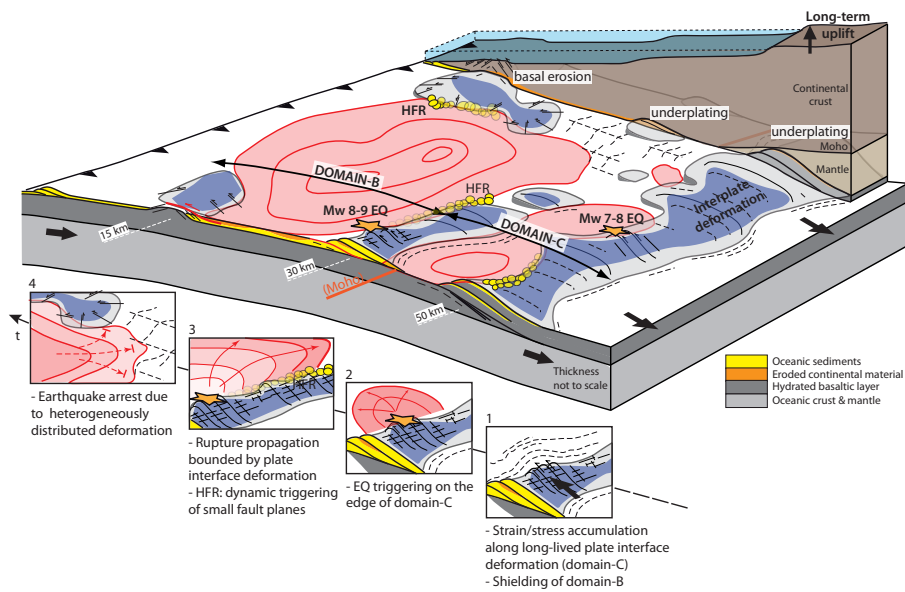
Figure 7. 3D view onto the subduction plate interface depicting the mutual spatial relationships between earthquake ruptures (in red) and longer-lived deformation determined from the CTT analysis (blue patches). Stages 1-4 illustrate how this deformation controls the triggering and limits seismic ruptures. See text for further discussion.